

Imaging Solute Distribution in Capillary Electrochromatography with Laser Scanning Confocal Microscopy

Mark Lowry, Yan He, and Lei Geng*

Department of Chemistry, University of Iowa, Iowa City, Iowa 52242

A method for the direct observation of solute molecules interacting with a C18 stationary phase under real separation conditions in capillary electrochromatography (CEC) is investigated. The experiments were performed in a capillary electrochromatographic mode; however, the method and findings are useful both in CEC and reversed-phase liquid chromatography. The distribution of solute molecules in the packed capillary is directly imaged with laser scanning confocal fluorescence microscopy. Conventional imaging techniques produce images where the C18 silica beads cannot be distinctively identified as a result of the deep depth of field. The optical sectioning capability of confocal imaging overcomes this problem to afford clearly defined images of the stationary-phase packing and the surrounding mobile phase. Fluorescein molecules are preferentially distributed in the mobile phase under reversed-phase chromatographic conditions. Nile Red and rhodamine 6G molecules prefer the environments of the porous C18 beads. Intensity distributions over time for areas within the stationary-phase beads differ from distributions of areas outside the beads in the mobile phase. Images taken at different depths into the capillary probe the internal structure of the C18 beads. While the internal structures of most beads are porous, confocal images show a small fraction (2%) of the silica beads have porous shells and nonporous cores. The capability of imaging the stationary phase distinctively from the mobile phase opens the possibilities of studying the quality of stationary phase, the structure of the column packing, and the mechanisms of separation.

Direct observation of the molecular distribution and molecular processes in separation columns has been a dream in chemical separations. Direct visualization will allow examination of the density and homogeneity of the packing that affects the efficiency of chromatographic separations. On the molecular level, direct observation of the stationary phase will enable studies of diffusion, partitioning, and sorption processes at the chromatographic interface. The separation efficiency can be directly traced back to the column—the structure of the packed stationary phase and its interaction with the solute molecules. To achieve direct observation of molecular processes, the imaging technique needs

to have high spatial and temporal resolution, with high sensitivity. High spatial resolution is required to resolve the stationary phase from the mobile phase and to probe the local environments within individual chromatographic beads. Millisecond time resolution is needed to follow chemical separations in real time and to enable kinetic studies of the adsorption/desorption processes.

Several imaging techniques have been utilized to visualize separation columns. Surface imaging techniques, such as atomic force microscopy (AFM), reveal the surface morphology of the stationary-phase beads with high spatial resolution.¹ However, it is not possible to obtain chemical and kinetic information using these imaging techniques under real chromatographic conditions. NMR imaging has been used as a noninvasive technique to observe the migration of chromatographic bands in the column and inhomogeneities in the packed bed.^{2–6} It is based on the reduction of relaxation times of protons by nearby gadolinium ions in the solution. The spatial resolution of NMR imaging is on the order of tens to hundreds of micrometers, and its slow time resolution does not allow studies of kinetic sorption processes. More recently, Guiochon and co-workers used direct photographic imaging to visualize band migration in chromatography.⁷ An iodine band is injected into the column and migrates as high pressure is applied. Photographs taken at various times after sample injection reveal the evolution of band shapes as the separation proceeds. Photographic imaging has uncovered invaluable information on chromatographic retention that was not available previously. In a series of work, they investigated the iodine band shapes, wall effects, viscous fingering, influence of inlet frit diameter and porosity on the flow profiles, and radial distributions of velocities in chromatographic separations.^{7–15} The spatial

- (1) Shakesheff, K. M.; Davies, M. C.; Jackson, D. E.; Roberts, C. J.; Tendler, S. J. B.; Brown, V. A.; Watson, R. C.; Barrett, D. A.; Shaw, P. N. *Surf. Sci.* **1994**, *304*, L393–L399.
- (2) Bayer, E.; Muller, W.; Ilg, M.; Albert, K. *Angew. Chem., Int. Ed. Engl.* **1989**, *28*, 1029–1032.
- (3) Bayer, E.; Baumeister, E.; Tallarek, U.; Albert, K.; Guiochon, G. *J. Chromatogr., A* **1995**, *704*, 37–44.
- (4) Tallarek, U.; Baumeister, E.; Albert, K.; Bayer, E.; Guiochon, G. *J. Chromatogr., A* **1995**, *696*, 1–18.
- (5) Aime, S.; Botta, M.; Ermondi, G. *J. Magn. Reson.* **1991**, *92*, 572–580.
- (6) Tallarek, U.; van Dusschoten, D.; Scheenen, T.; Van As, H.; Bayer, E.; Guiochon, G.; Neue, U. D. *AIChE J.* **1998**, *44*, 1962–1975.
- (7) Shalliker, R. A.; Broyles, B. S.; Guiochon, G. *Anal. Chem.* **2000**, *72*, 323–332.
- (8) Broyles, B. S.; Shalliker, R. A.; Guiochon, G. *J. Chromatogr., A* **2001**, *917*, 1–22.
- (9) Shalliker, R. A.; Broyles, B. S.; Guiochon, G. *J. Chromatogr., A* **2000**, *888*, 1–12.

* Corresponding author: (phone) (319)-335-3167; (fax) (319)-335-1270; (e-mail) Lei-Geng@uiowa.edu.

resolution of this photographic imaging technique is a few tens to a few hundreds of micrometers. The resolution can be improved by digitizing at higher resolution; however, it is ultimately determined by the depth of field.

Fluorescence imaging is an excellent method for the direct observation of solute molecules in chemical separation due to its high sensitivity. Tsuda et al. examined electroosmotic flow profiles in a square channel by using a CCD camera to image a flowing fluorescent solution.¹⁶ Taylor and Yeung observed the flow shape in separation capillaries using solutions containing fluorescent latex microspheres or flowing fluorescent solutions.¹⁷ A light microscope equipped with a CCD camera was used to obtain a depth of field of $\sim 20\ \mu\text{m}$. Paul et al. also used laser-induced fluorescence microscopy for the imaging of pressure and electrokinetically driven flows in open capillary tubes.¹⁸ The technique uses a UV laser to release a caged fluorescent dye. The free fluorescent dye is excited with pulsed visible light, and the flow is tracked using a CCD camera. Fluorescence detection systems for capillary separations in which a CCD camera images a long section of an axially illuminated capillary have been developed and used in the evaluation of isoelectric focusing, capillary electrophoresis (CE), and isotachophoretic preconcentration in CE.^{19–27} In this method, laser excitation is used to excite a long portion of the capillary and a CCD detector collects a series of emission profiles in real time. This method has also been used to study molecular distributions in a packed capillary. Behnke and co-workers investigated frit effects in capillary separations.²⁸ Adsorption of analytes onto frits made of both sintered normal-phase silica and sintered reversed-phase silica was observed using this technique.

These pioneering works have provided a wealth of information on separation processes in CE and in RPLC. The application of

conventional fluorescence imaging to chromatographic separation, however, is limited by the large depth of field of the technique. For example, silica beads deep in the stationary phase cannot be distinctively observed because their sizes are smaller than the depth of field of the image. It is thus impossible to directly study the distribution of the solute molecules and their interactions with the stationary phase.

The retention mechanism in reversed-phase liquid chromatography (RPLC) has been an active field of study in chromatography for the past two decades.^{29–42} The organization of the stationary phase, diffusion of solute molecules, and interaction between solutes and the stationary phase have been intensively investigated with spectroscopic and imaging methods. Using single-molecule fluorescence spectroscopy, Wirth and co-workers observed both strong and weak adsorption of 1,1'-dioctadecyl-3,3,3',3'-tetramethylindocarbocyanine perchlorate (DiI) molecules onto the silica surface. AFM confirmed that the adsorption sites are defects or scratches on the silica surface and established for the first time that the active silanols are associated with the topology of the surface.^{29–31} Using total internal reflection fluorescence correlation spectroscopy, Hansen and Harris presented a very detailed kinetic picture of the adsorption/desorption processes at the chromatographic interface.³² Xu and Yeung observed electrostatic interactions between single protein molecules and fused-silica surfaces.³³ These interactions are related to chromatographic retention.

Many of these experiments were performed on model systems: unmodified or C18-derivatized flat silica surfaces. It is of interest to observe the diffusion, partition, and adsorption of solute molecules in real chromatographic columns with packed stationary phase, under real separation conditions.

In this article, we report the imaging of packed columns in CEC using confocal microscopy. With the superior spatial resolution of confocal imaging, the solute distribution between the stationary phase and mobile phase is clearly visualized. The distribution behavior of charged and hydrophobic solutes is studied. The heterogeneity of the stationary phase has been observed. Detailed analysis of confocal time-series images provides direct information to investigate solute partition and adsorption in the C18 chromatographic interfaces.

EXPERIMENTAL SECTION

Chemicals. Fluorescein disodium salt was purchased from EM Science (Gibbstown, NJ). Nile Red was obtained from Acros

- (10) Broyles, B. S.; Shalliker, R. A.; Guiochon, G. *J. Chromatogr., A* **2000**, 867, 71–92.
- (11) Shalliker, R. A.; Broyles, B. S.; Guiochon, G. *J. Chromatogr., A* **1999**, 865, 73–82.
- (12) Shalliker, R. A.; Broyles, B. S.; Guiochon, G. *J. Chromatogr., A* **1999**, 865, 83–95.
- (13) Broyles, B. S.; Shalliker, R. A.; Guiochon, G. *J. Chromatogr., A* **1999**, 855, 367–382.
- (14) Shalliker, R. A.; Broyles, B. S.; Guiochon, G. *J. Chromatogr., A* **1998**, 826, 1–13.
- (15) Broyles, B. S.; Shalliker, R. A.; Cherrak, D. E.; Guiochon, G. *J. Chromatogr., A* **1998**, 822, 173–187.
- (16) Tsuda, T.; Ikeda, M.; Jones, G.; Dadoo, R.; Zare, R. N. *J. Chromatogr.* **1993**, 632, 201–207.
- (17) Taylor, J. A.; Yeung, E. S. *Anal. Chem.* **1993**, 65, 2928–2932.
- (18) Paul, P. H.; Garguilo, M. G.; Rakestray, D. J. *Anal. Chem.* **1998**, 70, 2459–2467.
- (19) Sweedler, J. V.; Shear, J. B.; Fishman, H. A.; Zare, R. N.; Scheller, R. H. *Anal. Chem.* **1991**, 63, 496–502.
- (20) Paul, P. H.; Garguilo, M. G.; Rakestray, D. J. *Anal. Chem.* **1998**, 70, 2459–2467.
- (21) Johansson, J.; Johansson, T.; Nilsson, S. *Proc. SPIE* **1995**, 2629, 1–9.
- (22) Nilsson, S.; Johansson, J.; Mecklenburg, M.; Birnbaum, S.; Savanberg, S.; Wahlund, G.-G.; Moshbach, K.; Miyabayashi, A.; Larsson, P.-O. *J. Capillary Electrophor.* **1995**, 2, 46–52.
- (23) Wu, H.; Pawliszyn, A. *Am. Lab.* **1995**, 10, 48–52.
- (24) Johansson, J.; Witte, D. T.; Larsson, M.; Nilsson, S. *Anal. Chem.* **1996**, 68, 2766–2770.
- (25) Culbertson, C. T.; Jorgenson, J. W. *Anal. Chem.* **1998**, 70, 2629–2638.
- (26) Wu, J. Q.; Tragas, C.; Watson, A.; Pawliszyn, J. *Anal. Chim. Acta* **1999**, 383, 67–78.
- (27) Beale, S. C.; Sudmeier, S. J. *Anal. Chem.* **1995**, 67, 3367–3371.
- (28) Behnke, B.; Johansson, J.; Bayer, E.; Nilsson, S. *Electrophoresis* **2000**, 21, 3102–3108.

- (29) Wirth, M. J.; Swinton, D. J. *Anal. Chem.* **1998**, 70, 5264–5271.
- (30) Wirth, M. J.; Ludes, M. D.; Swinton, D. J. *Anal. Chem.* **1999**, 71, 3911–3917.
- (31) Swinton, D. J.; Wirth, M. J. *Anal. Chem.* **2000**, 72, 3725–3730.
- (32) Hansen, R. L.; Harris, J. M. *Anal. Chem.* **1998**, 70, 4247–4256.
- (33) Xu, N. X.; Yeung, E. S. *Science* **1998**, 281, 1650–1653.
- (34) He, Y.; Geng, L. *Anal. Chem.* **2001**, 73, 5564–5575.
- (35) McGuffin, V. L.; Chen, S.-H. *Anal. Chem.* **1997**, 69, 930–943.
- (36) Doyle, C. A.; Vickers, T. J.; Mann, C. K.; Dorsey, J. G. *J. Chromatogr., A* **1997**, 779, 91–112.
- (37) Rutan, S. C.; Harris, J. M. *J. Chromatogr., A* **1993**, 656, 197–215.
- (38) Lochmuller, C. H.; Colborn, A. S.; Hunnicutt, M. L.; Harris, J. M. *Anal. Chem.* **1983**, 55, 1344–1348.
- (39) Lochmuller, C. H.; Colborn, A. S.; Hunnicutt, M. L.; Harris, J. M. *J. Am. Chem. Soc.* **1984**, 106, 4077–4082.
- (40) Wang, H.; Harris, J. M. *J. Am. Chem. Soc.* **1994**, 116, 5754–5761.
- (41) Wang, H.; Harris, J. M. *J. Phys. Chem.* **1995**, 99, 16999–17009.
- (42) He, Y.; Geng, L. *Anal. Chem.* **2002**, 74, 1819–1823.

Organics (Morris Plains, NJ). Rhodamine 6G was purchased from Aldrich (Milwaukee, WI). HPLC grade acetonitrile was purchased from Fisher (Fair Lawn, NJ). The Luna C18 modified silica beads used in the CEC packing were obtained from Phenomenex (Torrance, CA). They have an average particle size of 10 μm , surface coverage of 17.5%, and average pore size of 100 Å. The coverage of bonded phase is 3.00 $\mu\text{mol}/\text{m}^2$. Deionized water was purified with a MilliQ system (MilliQ-Plus, Millipore, Bedford, MA) and was used to prepare all aqueous solutions. Three mobile-phase compositions were used: a mobile phase containing 80% acetonitrile and 20% borate buffer at a concentration of 4 mM and pH 8.5, a second containing 80% acetonitrile and 20% phosphate buffer at a concentration of 4 mM and pH 7, and a third consisting of 100% 4 mM borate buffer at a pH of 8.5. Refractive index matching oil ($n = 1.51$) was obtained from Carl Zeiss Microimaging, Inc. (Thornwood, NY). Polyimide-coated capillaries (50- μm i.d., 360- μm o.d.) and 400- μm -i.d. quartz tubing was acquired from Polymicro Technologies (Phoenix, AZ).

Capillary Electrochromatography. The packing of a quartz cell with C18 silica beads has been described previously.^{34,42} Briefly, a capillary ~ 50 cm in length was conditioned with 0.1 M NaOH for 20 min. The capillary was then thoroughly rinsed with purified water and dried with vacuum before it was sectioned into two parts. The end of one part was pressed into a paste of sodium silicate to take up a few millimeter length of the material. A thermal wire stripper was used to heat the sodium silicate to form a frit at the end of the capillary. The process was repeated for the other section of capillary. The fritted end of one capillary was then inserted into a 400- μm -i.d. quartz cell. A nonfluorescent adhesive was used to bond the capillary to the quartz cell. C18 modified silica beads were packed into the quartz cell before the second capillary was attached to it. The separation capillary now consisted of a quartz cell packed with C18 bonded phase with two lengths of capillary on either end of the cell (Figure 1A). The length of the packing was 1.0–1.5 cm. A power supply manufactured by Spelman (model CZE1000PN30, Hauppauge, NY) provided the high voltage in capillary electrochromatography (CEC). The current was continuously monitored with a picoammeter (model 486, Keithley Instruments Inc., Cleveland, OH). A syringe pump was used to rinse the column with mobile-phase solution between experiments. The capillary was conditioned with the mobile phase for at least 50 column volumes before the solute solution was injected.

Confocal Imaging. Confocal imaging of CEC was performed on an inverted confocal microscope (Axiovert 100, LSM 510 scan module, Carl Zeiss Inc., Thornwood, NY). The setup for imaging of the CEC column is shown in Figure 1B. The packed capillary was placed between a standard glass microscope slide and a coverslip supported by two spacers consisting of short pieces of quartz tubing. The capillary was surrounded by refractive index-matching fluid and care was taken to ensure that the coverslip sat level, directly on the quartz spacers. Refractive index matching is essential to obtaining an undistorted image with a narrow depth of field. This is accomplished by reducing refraction and scattering from the capillary walls. The fluid also promotes heat transfer, helping to eliminate temperature gradients.

The capillary, fixed between the two slides, was placed on the microscope stage with the packed zone directly over the objective.

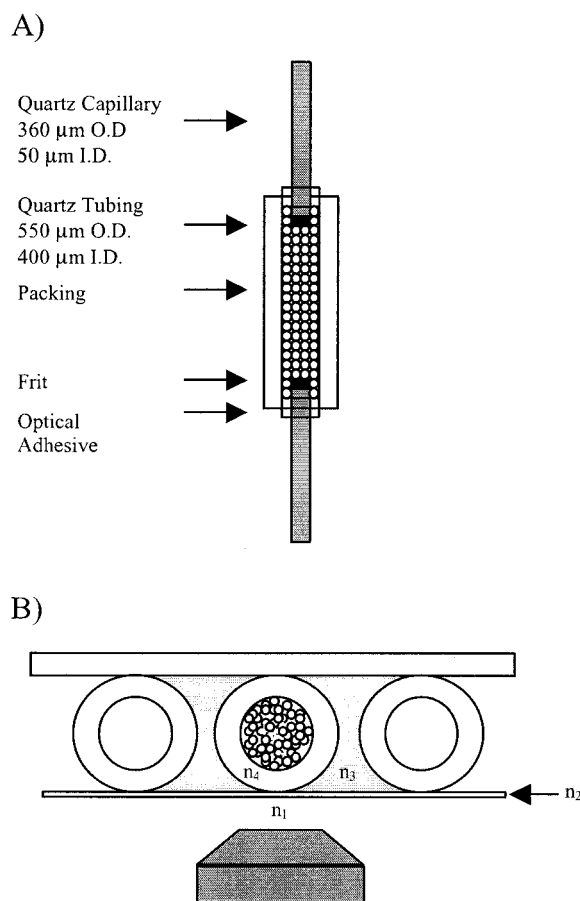


Figure 1. (A) Schematic diagram of packed capillary column. (B) Setup for imaging inside the packed column to reduce distortions caused by the curved interface. $n_1 = 1.00$ with the 20 \times (0.5 NA) dry objective or 1.51 with the 40 \times (1.3 NA) oil immersion objective. $n_2 = 1.51$ for the glass coverslip. $n_3 = 1.51$ for immersion oil. $n_4 = 1.46$ for quartz. Diagrams are not shown to scale.

One end of the capillary was placed in the inlet reservoir containing a solution of the fluorescent probe and the other in a reservoir containing only the mobile-phase solution. The inlet and outlet reservoirs were kept at the same heights.

An argon ion laser (Lasos, LGK 7812 ML1) and helium–neon laser (Uniphase, 1674P) provided excitation at 488 and 543 nm, respectively, with laser power regulated by acoustooptical tunable filters. A 40 \times (NA 1.3) oil immersion objective or a 20 \times (NA 0.5) objective was used. The scanning directions were rotated until the sides of the scanned area were parallel to the axis of the capillary. The spectral range of fluorescence emission was selected using the appropriate band-pass or long-pass filter. Fluorescence was directed through an adjustable pinhole and detected by a photomultiplier tube. The stored images were converted into text files with programs provided by the Image Analysis Facilities of the University of Iowa. The masks that determined regions of stationary phase and mobile phase in the images were manually defined in Adobe Photoshop (Adobe Systems Inc., San Jose, CA). Subsequent data and image manipulation was performed with programs written in MatLab (Mathworks, Inc., Natick, MA).

RESULTS AND DISCUSSION

The improved optical resolution of confocal imaging is illustrated with a solution of 100 μM Nile Red in 80% acetonitrile

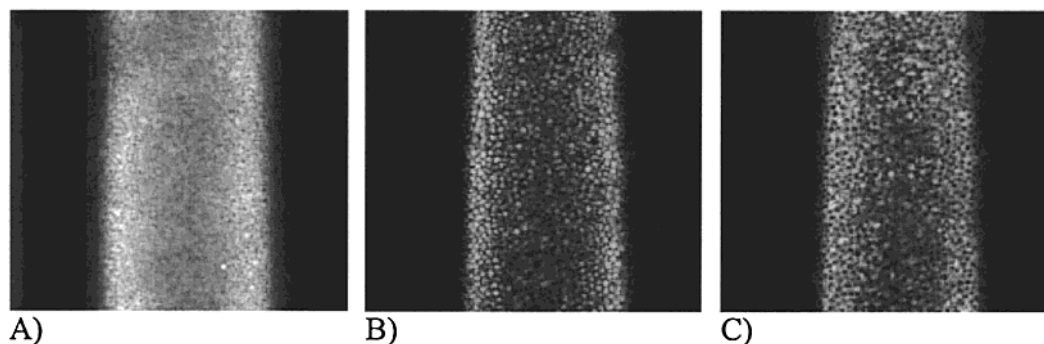


Figure 2. Confocal images demonstrating the ability to distinguish between the mobile phase and stationary phase in a packed column. (A) Image of 100 μM Nile Red. Optical slice thickness 10 μm . (B) Image of 100 μM Nile Red. Optical slice thickness 3.3 μm . (C) Image of 100 μM fluorescein. Optical thickness 3.3 μm . All images are 512 \times 512 pixels (460.6 $\mu\text{m} \times$ 460.6 μm).

with 20% 4 mM borate buffer at pH 8.5. With an optical slice of 10 μm collected using a 20 \times objective, the packed column appears as a blurred image where fluorescence from multilayers of beads at various depths in the packed bed mixes with mobile-phase emission. The silica beads can be observed as blurred shadows in the image upon close examination (Figure 2A). It is impossible to identify areas where the fluorescence is predominantly from solute molecules in the stationary phase and thus to extract the distribution of the solute molecules between the mobile and stationary phases. At a reduced pinhole size, thinner optical sections were acquired, producing sharply resolved images of the C18 beads in the packed bed. Figure 2B shows a confocal image of 100 μM Nile Red at the same mobile-phase conditions with an optical slice of 3.3 μm . Individual beads are clearly resolved, displaying much higher average intensity than pixels corresponding to the solution phase. This suggests substantial retention of Nile Red molecules in the hydrophobic C18 phase in this mobile-phase composition. Fluorescein molecules interact very differently with the stationary phase as expected. Figure 2C shows an image of 100 μM fluorescein in the same mobile phase with an optical slice of 3.3 μm . Fluorescein displays higher intensities in the solution than in the silica beads. At pH 8.5, the charged fluorescein molecules are preferentially distributed in the mobile phase. Nile Red and fluorescein can thus be separated in CEC based on their interactions with the stationary phase and their charges.

Figure 3 shows images collected at different depths of focus for a solution of 100 μM Nile Red with the same mobile-phase conditions as above. The thickness of the optical slice remained 3.3 μm , and images were collected using a 20 \times objective. The microscope objective was controlled to provide a series of z-section images at a step size of 1.65 μm . Selected images at a fixed interval (every fourth image) are shown in Figure 3. The first image shows an overall intensity profile that is most intense at the center of the cross section and decreases gradually near the walls. As the z-sectioning steps deeper into the packed capillary, portions of the cross section near the walls show the highest fluorescence intensity while the center portion becomes dimmer. When the excitation beam traverses the packed zone, substantial scattering occurs at the surface of the porous silica beads, resulting in a loss of excitation intensity. The loss increases with the depth through which the laser is probing. Fluorescence emission from deeply packed beads also needs to pass through layers of packing to reach the detector, again suffering from scattering losses at the interfaces. Image of Figure 3F was taken at a depth that is

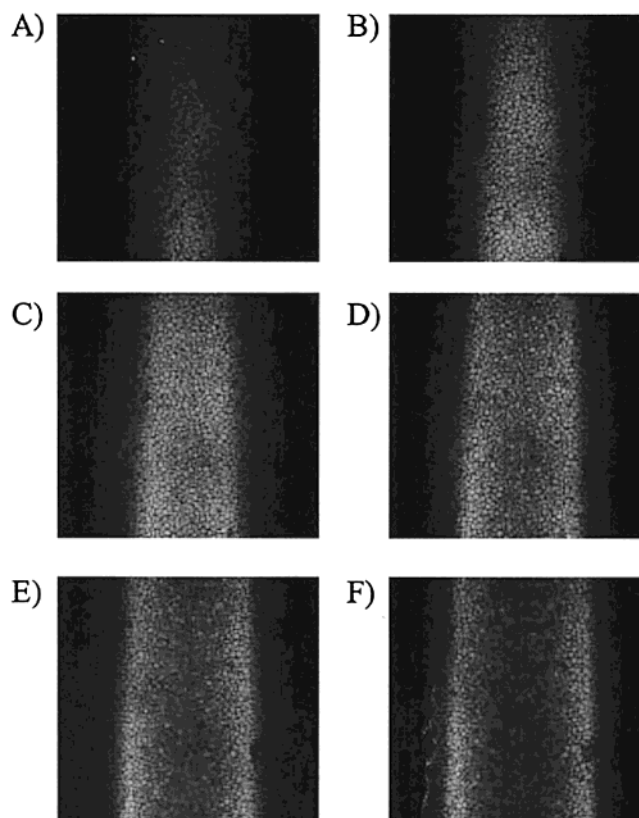


Figure 3. z-Section images of a packed column containing 100 μM Nile Red. Optical slice thickness 3.3 μm . z-Direction step size is 1.65 μm . Every fourth image is shown. All images are 512 \times 512 (460.6 $\mu\text{m} \times$ 460.6 μm).

33.3 μm from the first cross section. With 10 μm as the average size of the silica beads, the focal plane has passed through as many as three beads at the center of the cross section. Beads furthest away from the axis of the packed cell are imaged with the highest signal-to-noise ratios. Beads nearer the center portion of the cross sections, as the focus reaches further into the packed bed, remain defined (they can be seen with clear boundaries when the contrast of image 3F is adjusted to highlight the center of the cross section), but at lower SNR. The typical packed column used in CEC has a 50- μm i.d. Thus, the optical sectioning capability demonstrated here is sufficient to study the solute distribution at all radial positions in a capillary of this dimension.

The C18 modified silica beads were found to be heterogeneous. The beads are nonuniform in both size and structure. Images of

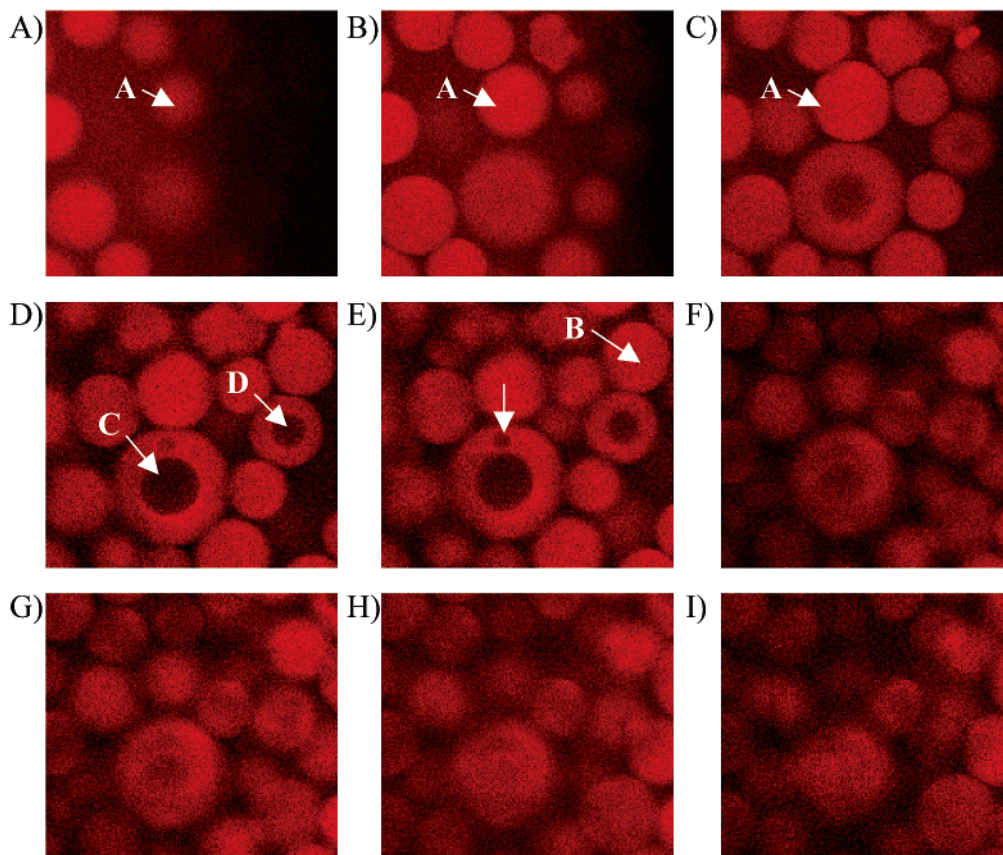


Figure 4. z-Section images of a packed column containing 10 μM rhodamine 6G at an optical slice thickness of 1.0 μm . z-Direction step size 0.50 μm . Every fifth image is shown. 512 \times 512 (115.2 $\mu\text{m} \times$ 115.2 μm) images are cropped to 157 \times 131 (35.3 $\mu\text{m} \times$ 29.5 μm) to show the area of interest in greater detail. Four beads of special interest are labeled (A–D) and discussed further in the text. Beads A and B are examples of beads with porous inner cores. Beads C and D show a nonporous inner structure with a porous outer shell. The arrow in image E indicates a second nonporous region within the porous outer shell of bead C.

10 μM Nile Red in 80% acetonitrile with 20% 4 mM phosphate buffer at pH 7 collected using a 40 \times (NA 1.3) oil immersion objective are shown in Figure 4. The optical slice is 1.0 μm thick. With the higher spatial resolution provided by this objective, the images are much sharper. The microscope objective was controlled to provide a series of z-section images at a step size of 0.5 μm with selected images shown at a fixed interval (every fifth image) in Figure 4. The size of a bead cannot be determined from a single cross section since the focal plane could be sectioning through the top or bottom portion of the bead instead of the center. The size can be reliably determined by examining many consecutive z-sections at different depths (images A–E in Figure 4) and finding the diameter of the largest image for a particular bead. In image 4A, the diameter of bead A appears to be \sim 26 pixels (5.72 μm), and in image 4B, it is estimated to be 43 pixels (9.46 μm), but the true diameter is determined to be 50 pixels (11.22 μm) from image 4C. By the same method, image 4E shows bead B to have a diameter of \sim 44 pixels (9.68 μm). Image 4D reveals bead C has a diameter of 73 pixels (16.06 μm). Such analysis has revealed the existence of size distribution of the silica beads.

More interestingly, the images show two distinctive types of beads. The majority of the beads are imaged as bright filled circles, for example, beads A and B as well as others in Figure 4. The solute molecules are retained in the C18 stationary phase, displaying a high intensity in the C18 phase and low intensity in

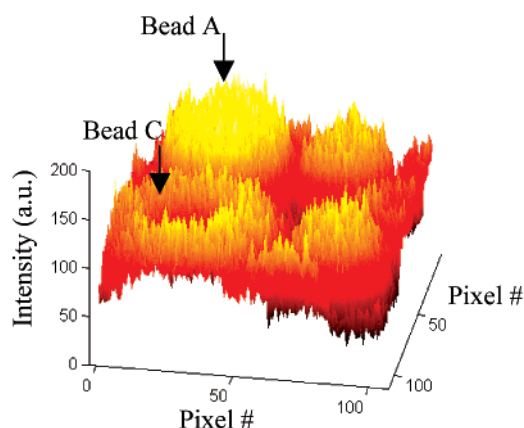


Figure 5. Three-dimensional intensity profile through the center plane of bead A from Figure 4C. Also shown is bead C.

the mobile phase. Figure 5 shows the three-dimensional intensity profile of a small area containing the center plane of bead A from Figure 4C. The intensity is highest within the porous silica beads and low in the mobile phase. The profile through the center plane of bead A is generally flat, indicating the porous structure of this type of bead is generally homogeneous. The pores in the porous silica tunnel deep into the beads to provide C18 phase throughout the bead, allowing solute molecules to penetrate. It displays a uniform distribution of solute molecules and, thus, uniform density

of the C18 phase. The solute can freely access any part of the bead, and the entire volume of the silica bead participates in the retention of the solute.

A small fraction of the silica beads, such as beads C and D in Figure 4, exhibit a heterogeneous solute distribution with a high-intensity shell and a dark core, suggesting a nonhomogeneous structure of the beads. In images 4A and 4B, bead C appears as a filled circle. When the laser steps into the bead, the image starts to show a donut shape. The hole in the donut becomes larger as the optical slice goes toward the center of the bead and shrinks again after it has passed through the center plane. Eventually, the image returns to a filled circle in image 4I. The inaccessibility of the core to the solute indicates a nonporous structure at the center. The bead is not completely nonporous as such a structure would allow only a monolayer of C18 on the surface of the bead. The optical image of the bead would have a spherical shell with a shell thickness equal to the resolution limit of confocal imaging. This is not the case. All the inhomogeneous beads display a shell that is between 1 and 3 μm thick. These beads clearly have a nonporous core and a porous outer shell. Moreover, bead B also shows an additional nonporous area within the porous outer shell, shown by an arrow in image 4E. The dimension of this nonporous volume is 11 pixels (2.42 μm). The fraction of heterogeneous beads was estimated from the entire set of z-section images partially shown in Figure 3. Out of ~ 1000 silica beads, 21 beads (2%) have a nonporous inner core.

We examined the capability of confocal imaging in providing information about the distributions of solutes in the C18 modified silica beads and in the mobile phase. As shown in Figure 2A, at a large depth of field, it is impossible to reliably investigate the molecular behavior of the solutes in the beads since the fluorescence signal at each pixel is a sum of contributions from the bead and the mobile phase. Thinner optical slices make it possible to investigate this distribution.

Stationary-phase beads are partially observed in the image of 10 μM rhodamine 6G, a cationic dye molecule, in 80% acetonitrile with 20% 4 mM phosphate buffer at pH 7 as bright regions in Figure 6A. Dark mobile-phase areas separate the individual beads. A portion of the selected bead was defined as five zones, A–E, from the center portion of the bead to the interface between the bead and the mobile phase, and one area, F, in the mobile phase as shown in Figure 6B. The image size was reduced to improve the time resolution of the measurements. The total time for collecting a single image was 12.2 ms with a 2-ms lag time before the next image was collected. The dwell time at each pixel in the image was 1.76 μs . The pinhole was set such that a 1.0- μm optical slice was collected using a 40 \times (NA 1.3) oil objective.

We examined 2500 consecutive time-series images of the packed capillary at a constant flow of rhodamine 6G. The intensity distributions throughout the time series of the zones defined in Figure 6B, including the mobile phase, were constructed and are plotted in Figure 6C. They are well described by a Gaussian distribution, and the results of fitting are shown in Table 1.

The solute concentration is low in the mobile phase due to its retention in the stationary phase. On average, there are fewer solute molecules in the mobile phase; thus, zone F displays an intensity profile that is centered at a low value of 87. The width (fwhm) of the distribution is 32. Zones A–C are well within the

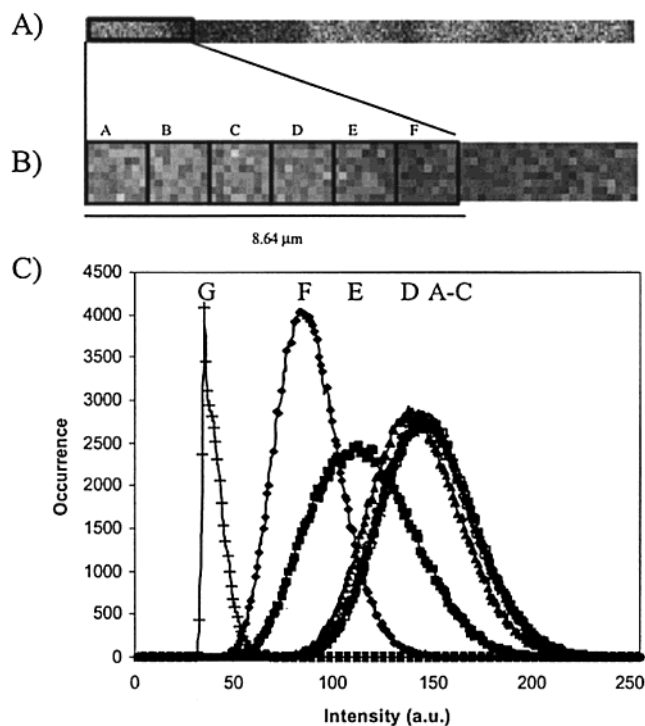


Figure 6. (A) Representative image of a packed column containing 10 μM rhodamine 6G. Optical slice thickness is 1.0 μm . Image size reduced to 256×8 ($46.1 \mu\text{m} \times 1.4 \mu\text{m}$) to increase time resolution. Stationary-phase beads appear as bright stripes with dark patches of mobile phase separating them. (B) Left portion of (A) containing both a portion of a C18 bead and a region of mobile phase. Six 8×8 ($1.4 \mu\text{m} \times 1.4 \mu\text{m}$) regions are defined. (C) Intensity distribution of regions defined in (B) integrated over time. Also plotted is the intensity distribution collected as mobile phase containing no rhodamine 6G passed through the column. Intensity distributions are well fitted by Gaussian functions. Fitting parameters are shown in Table 1.

Table 1. Fitting Parameters of Gaussian Intensity Distributions Shown in Figure 6

zone	center ^a	SD ^b	width ^a	SD ^b	R ²
A	146.3	0.1	46.4	0.2	0.997
B	147.3	0.1	46.3	0.2	0.997
C	146.7	0.1	46.2	0.2	0.997
D	140.8	0.1	45.3	0.2	0.996
E	113.7	0.2	52.5	0.4	0.993
F	86.6	0.1	31.6	0.2	0.994

^a Center: center of the Gaussian intensity distribution. Width: width of the Gaussian intensity distribution. ^b Standard deviations for centers and widths are shown.

bead and thus contain on average more solute molecules than zone F. They display similar intensity distributions centered at a much higher intensity of ~ 147 with a larger width of 46. The widths of these three areas are identical within the error of the fit and the center varies only slightly. As these areas are close to the center, the 1- μm optical slice samples a volume that is confined within the bead. The similar intensity distributions confirm the majority of detected signal from these regions originates from solute molecules within the C18 bead. The intensity distributions in these regions are thus characteristic of the solute distribution in the stationary phase since solute molecules in the mobile phase occupying the pores of the bead should contribute only a small

fraction of intensity within the bead. At location D, moving away from the center of the bead, slightly more fluorescence from the mobile-phase solution outside the bead is collected, resulting in the slight shift to a lower intensity centered at 141. Zone E is at the very edge of the bead. A significant portion of the probe volume now lies in the mobile phase. Less fluorescence is collected from within the bead. The intensity distribution is significantly broadened (fwhm 53) and shifted to a lower value centered at 114. The overlap of this broad distribution with the distributions both within the bead (zones A–D) and in the mobile phase (zone F) is consistent with a sampling of solute molecules in both the stationary and the mobile phases.

Figure 6 demonstrates that fluorescence intensities in the center fraction of the beads reliably report the solute distribution in the stationary phase. The similarity of the intensity profiles of zones A–C suggest a homogeneous solute distribution in the bead on a large scale of $1.4\ \mu\text{m} \times 1.4\ \mu\text{m}$.

The finite widths of the intensity distributions are interesting. They do not originate from the random noise in the fluorescence intensity measurement. Also shown in Figure 6C is the intensity distribution of zone F as mobile-phase solution in the absence of fluorescent probe flowed through the capillary. This set of time-series images was collected for the same area of focus by reversing the polarity after the rhodamine 6G flow had been imaged. Reversing the polarity reversed the direction of flow. The outlet vial containing mobile-phase solution thus became the inlet vial. At this point, the mobile-phase solution was contaminated with an extremely small amount of fluorescent probe (the rhodamine 6G that had moved through the capillary from the inlet vial into the outlet vial). The mobile-phase solution was not changed, however, due to difficulty in changing the solution without changing the location the capillary column, thus losing focus in the region of interest. The intensity distribution for the mobile-phase flow (distribution G in Figure 6C) is much narrower than the distributions of flowing rhodamine 6G and has been scaled down by a factor of 4 in order to be plotted on the same scale as distributions A–F. The pixel intensities of the image in the absence of the solute molecules are clustered in a very narrow range (centered at 39 with a fwhm of 10). Unlike the other distributions, this distribution is not well fit by a single Gaussian. What is important to note, however, is the narrow width and lack of significant overlap with the other distributions, indicating the finite widths discussed above are the result of solute distributions and not random noise.

The intensity distributions in Figure 6C are thus the manifestation of the solute distribution over both time (2500 images, 34.619 s) and space (8×8 pixels, $1.4\ \mu\text{m} \times 1.4\ \mu\text{m}$). We questioned whether the distributions were the result of certain pixels within each zone containing consistently more solute molecules due to their unique pore structure, stationary-phase structure, or solute–stationary-phase interaction. If this were the case, these unique pixels would be constantly higher in intensity. Each pixel would thus have a characteristic intensity level based on its unique pore structure. The collective intensity levels of all pixels in a region would form intensity distributions with a finite width seen in Figure 6C. To elucidate the question, the intensity distributions

Table 2. Fitting Parameters of Gaussian Intensity Distributions for Five Randomly Chosen Pixels

pixels	center ^a	SD ^b	width ^a	SD ^b	R ²
a	147.0	0.4	46.0	0.8	0.958
b	147.1	0.4	48.0	0.9	0.955
c	148.0	0.4	45.9	0.9	0.945
d	148.2	0.4	47.8	0.9	0.955
e	145.8	0.4	46.1	0.8	0.956

^a Center: center of the Gaussian intensity distribution. Width: width of the Gaussian intensity distribution. ^b Standard deviation for centers and widths are shown.

of all individual pixels throughout the time-series image were constructed. As with the larger regions shown in Figure 6, the distributions for individual pixels within the C18 bead show a finite width and are fit reasonably well by a Gaussian distribution. The centers and widths of these distributions are shown in Table 2. They are very similar in both center and width and they do not vary significantly from the fits for the larger areas shown in Figure 6. This suggests that the intensity distributions are not caused by structural differences between individual pixels, but rather by the random distribution of solute molecules in the C18 beads over time.

Figure 7 shows images collected as 10 μM fluorescein in 100% 4 mM borate at pH 8.5 flowed through the packed capillary. Images were collected using a $20\times$ objective with an optical slice of $3.3\ \mu\text{m}$. A time series consisting of 750 consecutive images at a time resolution of 230 ms/image with a lag time of 237 ms between images was collected. Fluorescein is not as heavily retained in the C18 stationary phase as Nile Red. The confocal images display intensities higher in the mobile phase than in the silica beads. The center fraction of a bead is magnified and displayed in Figure 7B. Some pixels have higher intensities and thus more solute molecules than others during the pixel integration time of $1.76\ \mu\text{s}$. Eight of the magnified images were randomly selected in time and are displayed in Figure 7B. It is evident that the bright spots are (1) smaller than the size of a pixel, (2) randomly distributed in the bead, and (3) randomly “migrate” throughout the bead over time. Bright areas that connect many pixels are not observed, indicating that the solute molecules are not clustered in regions that are larger than the resolution limit of confocal imaging. The uniform spatial and temporal distribution of the high-intensity pixels suggests that there are not special surface areas in the stationary phase that strongly retain the solute molecules. In other words, if the strong retention sites exist, they must be of a size smaller than the optical resolution of a few hundred nanometers. The distribution of these strong sites is homogeneous in the beads upon visual inspection.

Another possibility exists that the events of strong retention do not occur constantly at such a strong retention site. The solutes are “weakly” retained at these sites most times but get strongly retained during a small fraction of time. Time correlation analysis for individual pixels has shown that such retention events do not occur over the time resolution of these confocal images. In other words, the time constants for these events are shorter than 467 ms for fluorescein in 100% borate buffer.

Experiments are under way to probe the solute distribution of various probes at different mobile-phase compositions and at low

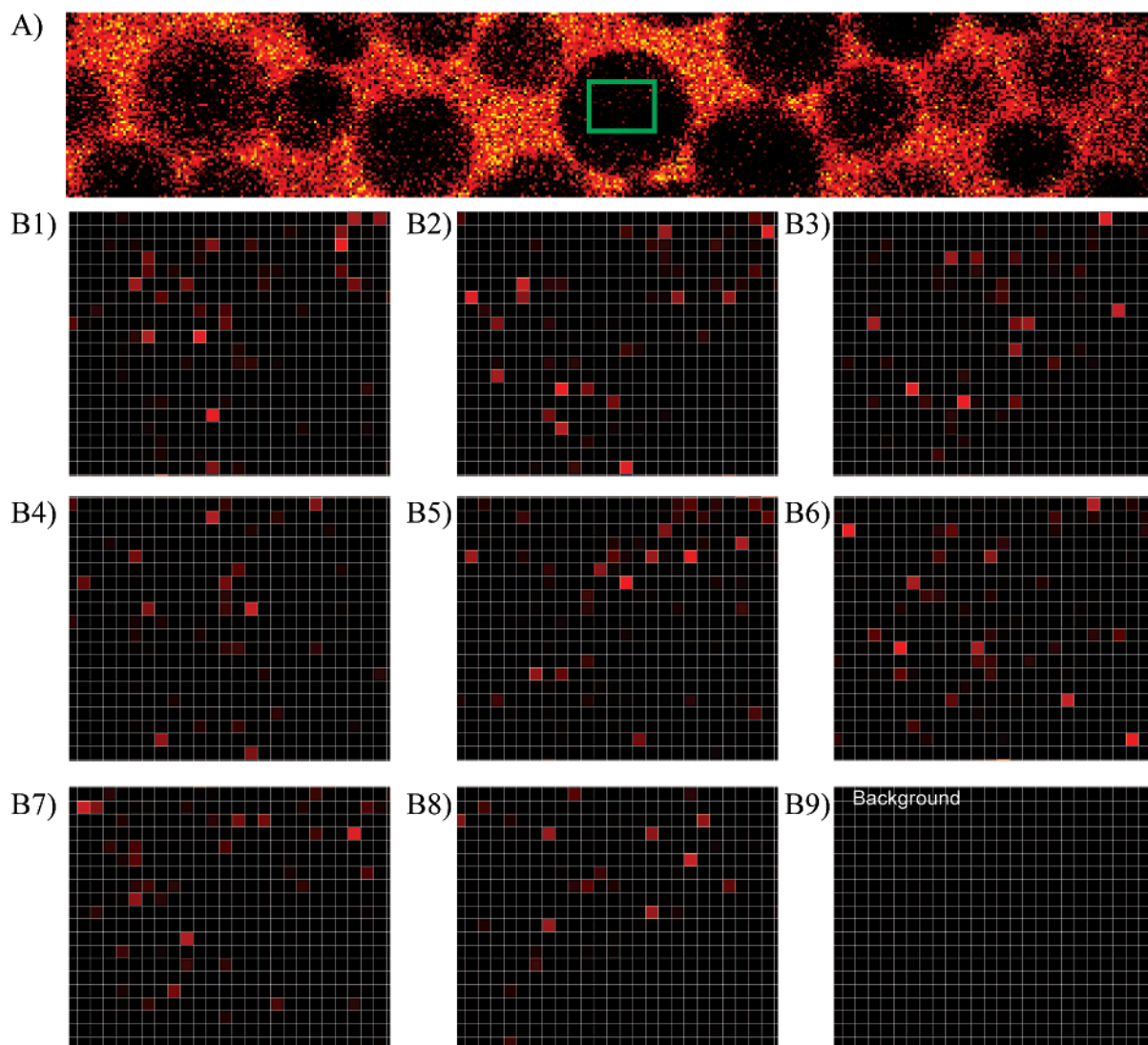


Figure 7. (A) Representative time-series image of a packed column containing 10 μM fluorescein. Optical slice thickness is 3.3 μm . Image size reduced to 512×75 ($115.2 \mu\text{m} \times 16.8 \mu\text{m}$) to increase time resolution. Stationary-phase beads appear as dark spots in a bright background of mobile phase. (B) The 25×20 pixel ($5.5 \mu\text{m} \times 4.4 \mu\text{m}$) region indicated in (A) is magnified. Eight images randomly selected over time are displayed. The ninth background image was collected as mobile phase containing no fluorescein was passing through the column.

concentration with a higher time resolution and improved signal-to-noise ratio. This will allow mechanistic studies of the chromatographic retention at higher time resolution. The studies with confocal imaging will provide direct information to elucidate the solute partition and adsorption in the C18 chromatographic interfaces. With confocal imaging, we are directly observing kinetic processes in chromatographic separation, such as the formation and removal of air bubbles in CEC, the migration of silica beads under high voltage, and the wetting of nanopores in the stationary phase. Fluorescence correlation analysis of the confocal time-series

images reveals adsorption/desorption processes and the distribution of these adsorption sites in chromatographic stationary phase.

ACKNOWLEDGMENT

We gratefully acknowledge the University of Iowa, the Office of the Vice President for Research, for supporting this research.

Received for review November 8, 2001. Accepted January 30, 2002.

AC015680I